RESEARCH   **Open Access**

Dual-Horizon Peridynamics Analysis of Debonding Failure in FRP-to-Concrete Bonded Joints

Wanjin Li and Li Guo*

Abstract

A dual-horizon peridynamics (DH-PD) model is proposed for the simulation of debonding process in fiber-reinforced polymer (FRP)-to-concrete bonded joints. In the novel procedure of implementing DH-PD in the framework of finite element method (FEM), truss elements are employed to represent the bonds and dual-bonds. The quadtree approach is utilized to generate the multi-scale discretization and a volume correction scheme based on the background grid is proposed for the non-uniform grid. A benchmark numerical example is performed to test the accuracy and efficiency of the developed model in analysis of the bond behavior. The predicted results are consistent with the experimental findings, the FEM results and the analytical solutions. Additionally, these results demonstrate that the bond strength and the debonding ductility are visibly affected by concrete strength and the thickness of FRP plate, while the adhesive thickness has no significant impact on the debonding behavior.

Keywords: dual-horizon peridynamics, debonding simulation, FRP, concrete

1 Introduction

Fiber-reinforced polymer (FRP) is a kind of high performance material with high strength-to-weight ratio, good durability and ease of application. The external bonding of FRP to concrete members has been accepted as an effective technology to strengthen and retrofit concrete structures (Täljsten 1996; Ronagh and Baji 2014). In FRP strengthened concrete structures, the interfacial bond between FRP and concrete is often the weakest region and can contribute to the debonding failure. Therefore, ensuring the safety of FRP strengthened concrete structures necessitates a realistic description of the bond behavior.

Over the past two decades, extensive experimental studies have been conducted to investigate the bond behavior in FRP strengthened concrete structures. Generally, the shear tests of FRP-to-concrete bonded joints are the most commonly used test methodology, in which an FRP plate is bonded to a concrete prism and subjected to tension (Chen et al. 2001; Yao et al. 2005; Ali-Ahmad et al. 2006; Carrara et al. 2011; Benzarti et al. 2011; Wu and Jiang 2013; Kabir et al. 2017). Typical debonding failure in the shear test is observed generally in concrete at a few millimeters from the adhesive layer. Unfortunately, the data directly measured from the shear tests always have significant variations due to bending effect of the thin FRP plate and irregularity of aggregates in concrete. In order to reduce the scattering of the directly measured results, substantial analytical models were developed (Yuan et al. 2004; Dai et al. 2005; Zhou et al. 2010; Liu and Wu 2012; Pan and Wu 2014; Moein and Tasnimi 2016). However, because such analytical models are based on empirical parameter calibrations and the theory of elasticity, they are limited to describe the nonlinear debonding process.

Apart from experimental and analytical studies, the numerical simulation is a convenient and powerful alternative for the study of the interfacial bond. In current available numerical methods, finite element method

*Correspondence: lguo@seu.edu.cn
Jiangsu Key Laboratory of Engineering Mechanics, Department of Engineering Mechanics, School of Civil Engineering, Southeast University, Nanjing 210096, China

(FEM) is generally used and existing FEM studies can be classified into two approaches. One approach is the interface modeling approach, in which the bond behavior is modeled using a layer of interface elements (Diab and Wu 2007; Chen et al. 2011; Sun et al. 2017a, b). The other is the direct modeling approach, in which debonding is simulated by modeling the failure of concrete adjacent to the adhesive layer (Lu et al. 2005a, 2006; Pham and Al-Mahaidi 2007; Tao and Chen 2015; Xu et al. 2015). The success of the former approach depends on the constitutive law of the interface elements; as a result, it is not truly predictive. In the latter approach, the principle of equivalent stiffness, namely the thickness of the FRP plate is amplified and the modulus of elasticity is modified to keep the axial stiffness of FRP constant, is often utilized to enlarge the size of elements in FEM model. Consequently the computational cost is significantly reduced, however, the equivalence can trigger numerical errors. Additionally, in FEM, singularities in the presence of discontinuities caused by cracks usually are unavoidable, which makes the construction of a corresponding numerical model cumbersome and time-consuming.

Alternatively, a new non-local method of continuum called peridynamics (PD) has been developed by Silling (2000), Silling et al. (2007) to overcome the limitations of traditional FEM. PD employs spatial integral equations rather than partial differential equations, making it more suitable for solving practical problems involving discontinuities and significant non-local effects. It has been applied successfully to a wide range of traditional problems including crack propagation in brittle materials (Ha and Bobaru 2011), the fracture of concrete structures (Li and Guo 2018), composites delamination (Hu et al. 2012), thermal diffusion (Bobaru and Duangpanya 2012) and flow in porous media (Jabakhanji and Mohtar 2015).

In the original PD formulation developed by Silling, the discretization is uniform and the horizon sizes are constant in the whole domain. However, heterogeneous materials and structures, such as FRP strengthened concrete structures necessitate the non-uniform and multi-scale discretization to model different constitutive materials separately and reduce the computational cost. Recently, a dual-horizon peridynamics (DH-PD) formulation was proposed by Ren et al. (2016) and Rabczuk and Ren (2017) to incorporate non-uniform material point distribution and variable horizons into PD. DH-PD can completely solve the issues of spurious wave reflections and simulate the crack propagation in composite materials. Therefore, DH-PD is suitable for simulating debonding failure of FRP strengthened concrete structures.

In present paper, DH-PD is extended and applied for investigating debonding failure in FRP-to-concrete bonded joints. To keep the efficiency of FEM without losing the generality of DH-PD, DH-PD is implemented in the framework of FEM and the quasi-static simulations are carried out by solving the equilibrium equations. Furthermore, in order to reduce the computational cost and increase the accuracy, a non-uniform discretization and a volume correction scheme are proposed. The remainder of the paper is organized as follows. Section 2 is devoted to a brief review of PD and DH-PD. In Sect. 3, the numerical implementation of DH-PD within the framework of FEM is proposed. In Sect. 4, a DH-PD model of FRP-to-concrete bonded joints is established and a comparison between DH-PD predictions with test results is carried out to validate the proposed method on debonding failure. In Sect. 5, the effects of concrete strength, the FRP thickness and the thickness of the adhesive layer on the bond behavior are evaluated. Finally, some concluding remarks are addressed in Sect. 6.

2 Theoretical Basis of Peridynamics
2.1 Basic Equations of PD and Constitutive Modeling
Peridynamics is a non-local continuum theory, which assumes that every material point interacts with all others within its horizon. Horizon with radius of δ refers to the size of non-local interaction and such interaction is called bond. The PD equation of motion at a material point x in the continuum R_0 and time t is defined as

$$\rho(x)\ddot{u}(x,t) = \int_{H_x} f(x,x',u(x,t),u(x',t),t)\,\mathrm{d}V_{x'} + b(x,t)$$

(1)

where $f = f(x,x',u(x,t),u(x',t),t)$ is the pairwise force function of the bond xx', which describes the interactions between x and any point x' within its horizon, $H_x = \{x' \in R_0 | \,||x-x'|| \leq \delta\}$ is the horizon of material point x, $||\cdot||$ is the Euclidean norm, ρ is the density, u is the displacement, $\ddot{u}$ is the acceleration, $\mathrm{d}V_{x'}$ is the volume element, b is the prescribed loading force density.

For brittle micro-elastic materials, the pairwise force function f of the bond xx' is expressed as

$$f(u'-u, x'-x) = f(\eta, \xi) = (\eta+\xi)/||\eta+\xi||cs$$

(2)

where $\xi = x - x'$ and $\eta = u - u'$ denote the relative position and the relative displacement of material points at x and x' in the reference configuration, respectively; $\eta + \xi$ represents the current relative position between the material points; c is the micro-modulus function and denotes the stiffness of the bond. In present study, the two dimensional (2D) conical micro-modulus function is adopted, which takes the form of

$$c = 24E(1 - ||\xi||/\delta)/\left[\pi\delta^3(1-\nu)\right]$$

(3)

where E is Young's modulus; ν is Poisson's ratio, which is equal to 1/3 for a 2D continuum. s is the bond stretch, which is defined as

$$s = (||\boldsymbol{\eta} + \xi|| - ||\xi||)/||\xi|| \qquad (4)$$

In order to incorporate damage into the constitutive model, a critical bond stretch s_0 is introduced. Once the critical bond stretch is reached, the bond breaks and consequently the bond forces vanish. A history-dependent function μ is used to implement it, which is defined as

$$\mu(t,\xi) = \begin{cases} 1, & \text{if } s(t',\xi) < s_0, \ \forall 0 < t' < t, \\ 0, & \text{otherwise.} \end{cases} \qquad (5)$$

The local damage at material point $\boldsymbol{x}$ is defined as the ratio of the number of broken bonds to the total number of bonds relevant to point $\boldsymbol{x}$,

$$\varphi(\boldsymbol{x},t) = 1 - \left(\int_{H_{\boldsymbol{x}}} \mu(\boldsymbol{x},\xi,t)\mathrm{d}V_\xi\right) / \left(\int_{H_{\boldsymbol{x}}} \mathrm{d}V_\xi\right) \quad (6)$$

The value of $\phi(\boldsymbol{x}, t)$ ranges from 0 to 1. Zero denotes virgin material, while one indicates complete damage.

2.2 Dual-Horizon Peridynamics

In DH-PD formulation, the horizon H_x is still the neighborhood of material point $\boldsymbol{x}$ with the horizon radius of δ_x, where the bond $\boldsymbol{xx'}$ will exert the direct force $\boldsymbol{f_{xx'}}$ on $\boldsymbol{x}$. Based on Newton's third law, $\boldsymbol{x'}$ will suffer the reaction force $-\boldsymbol{f_{xx'}}$. The dual-horizon $H'_x = \{\boldsymbol{x'} \in R_0 | \boldsymbol{x} \in H_{\boldsymbol{x'}}\}$ is a set of points whose horizons contain $\boldsymbol{x}$. The bond from the dual-horizon is named as dual-bond. Similarly, the dual-bond $\boldsymbol{x'x}$ will exert the direct force $\boldsymbol{f_{x'x}}$ on $\boldsymbol{x'}$ and $\boldsymbol{x}$ will suffer the reaction force $-\boldsymbol{f_{x'x}}$. When uniform discretization and constant horizon are used, DH-PD reduces to the traditional PD (Ren et al. 2016). The equation of motion, the bond force and the dual-bond force in DH-PD are given as

$$\rho(\boldsymbol{x})\ddot{\boldsymbol{u}}(\boldsymbol{x},t) = \int_{H_{\boldsymbol{x}}} \boldsymbol{f_{xx'}}(\boldsymbol{\eta},\xi)\mathrm{d}V_{\boldsymbol{x'}}$$
$$+ \int_{H'_{\boldsymbol{x}}} -\boldsymbol{f_{x'x}}(-\boldsymbol{\eta},-\xi)\mathrm{d}V_{\boldsymbol{x'}} + \boldsymbol{b}(\boldsymbol{x},t) \qquad (7)$$

$$\begin{cases} \boldsymbol{f_{xx'}} = \mu c(\boldsymbol{x'},\delta_{\boldsymbol{x'}})s\frac{\boldsymbol{\eta}+\xi}{||\boldsymbol{\eta}+\xi||} \\ \boldsymbol{f_{x'x}} = -\mu c(\boldsymbol{x},\delta_{\boldsymbol{x}})s\frac{\boldsymbol{\eta}+\xi}{||\boldsymbol{\eta}+\xi||} \end{cases} \qquad (8)$$

Note that the micro-modulus $c(\boldsymbol{x}, \delta_{\boldsymbol{x}})$ depends on the horizon radius of material point $\boldsymbol{x}$ and takes half of the corresponding micro-modulus used in the constant-horizon PD. Furthermore, the bond and the dual-bond break independently considering that they may have different critical stretches.

3 Finite Element Discretization of Dual-Horizon Peridynamics

Macek and Silling (2007) pointed out that the basis equations of PD are consistent with FEM code architectures. Additionally, compared with FEM, PD and DH-PD are computationally expensive. Therefore, to gain the efficiency from FEM and exploit the generality of DH-PD, we implement DH-PD into the framework of FEM. The implementation process is comprised of two steps, namely, generating non-uniform grid and solving governing equations.

3.1 Non-uniform Grid

The value of horizon depends on the physical nature of the application being modeled (Silling and Askari 2005). In order to achieve acceptable accuracy, the horizon radius has to be determined in accordance with the lowest material point resolution locally required. However, the dense material point distribution and the sufficiently small horizon size can result in longer computational time. For sake of computational efficiency, non-uniform modeling is required, in which the regions of interest utilize dense material points and the other regions coarse material points.

The quadtree approach is one of the most popular algorithms to generate new material points in the implementation of multi-scale modeling, as shown in Fig. 1. Bobaru et al. (2009), Bobaru and Ha (2011) firstly introduced the quadtree approach in PD to implement the adaptive refinement process. Unfortunately, the so called hanging nodes are generated in their works, which would trigger the quadrature errors. Dipasquale et al. (2014) inserted new material points in a recursive manner at the mid points of the lines connecting adjacent material points of the same refinement level. The generation approach is simple. However, the properties of the interface material points, such as the shape and the size, are modified. Consequently, the properties of material points need to update, which is complex to implement, especially for the case of successive refinements. In present study, the quadtree approach is adopted, whereas the hanging nodes are eliminated. The details of the process are as follows.

Firstly, geometry of the specimen is meshed by uniform quadrate solid elements in commercial FEM software ABAQUS and the edge length is Δx. In what follows, we export the nodal data of the mesh and take the center (x_c, y_c) and the area of each element as the position and the associated area of the corresponding material point, respectively, as shown in Fig. 2a. If an element is refined, four sub-elements will be generated and their areas are one quarter of the original.
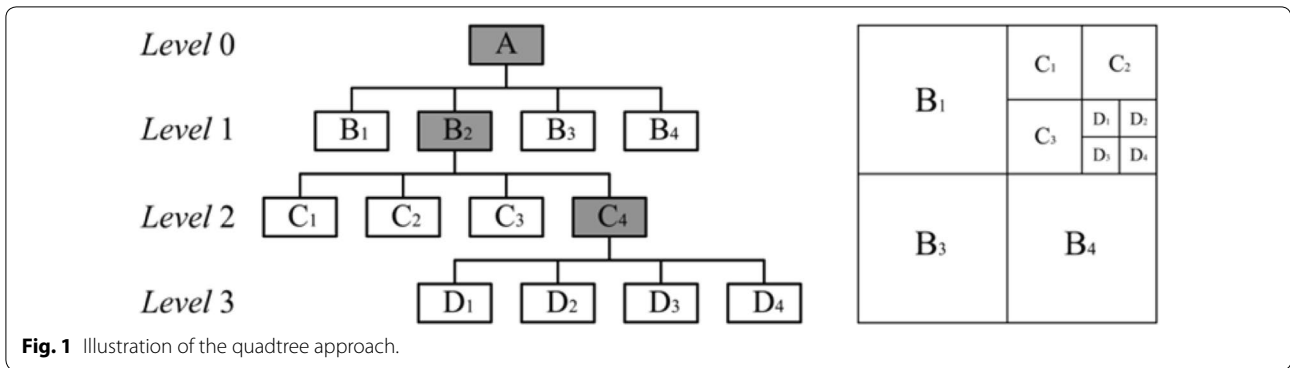
Fig. 1 Illustration of the quadtree approach.

Furthermore, the centers and vertexes of the sub-elements could be calculated from the center and vertexes of the original element. It can be noticed from Fig. 2b that the positions of all material points are at the centers of their associated domains, that is, the hanging nodes are not generated. In the same pattern, level 2 points can be generated from level 1 points, level 3 points from level 2 points and so on. Hence, the non-uniform discretization is obtained.

After discretization, the mesh of bonds are generated by a preprocessor in MATLAB, which connects each material point to all others within its horizon. The horizon of each material point is defined as three times the corresponding edge length.

3.2 Numerical Implementation
3.2.1 Volume Correction Scheme
For numerical purpose, the integral Eq. (7) is discretized into the following form

$$\rho \ddot{\boldsymbol{u}}_i = \sum_j^{N_{H_x}} \boldsymbol{f}_{ij}(\boldsymbol{\eta}, \xi, t)\Delta V_j + \sum_j^{N_{H'_x}} \left(-\boldsymbol{f}_{ji}(-\boldsymbol{\eta}, -\xi, t)\Delta V_j \right) + \boldsymbol{b}(\boldsymbol{x}_i)$$

(9)

where N_{H_x} is the number of material points included in the horizon of point $\boldsymbol{x}_i$; $N_{H'_x}$ is the number of material points whose horizons include point $\boldsymbol{x}_i$; ΔV_j is the portion of the volume of point $\boldsymbol{x}_j$ covered by the horizon of point $\boldsymbol{x}_i$. When uniform quadrate discretization is adopted, the volume of point $\boldsymbol{x}_j$ usually takes the value of $\Delta V_j = |\Delta x_j|^2$. Considering that some points are partially covered, a correction scheme of volume fraction for point $\boldsymbol{x}_j$ were proposed by Bobaru and Ha (2011) as

$$\Delta V_j = \begin{cases} \Delta V_j, & ||\xi|| \le \delta - 0.5\Delta x; \\ \frac{\delta + 0.5\Delta x - ||\xi||}{\Delta x}\Delta V_j, & \delta - 0.5\Delta x < ||\xi|| \le \delta + 0.5\Delta x; \\ 0, & ||\xi|| > \delta + 0.5\Delta x. \end{cases}$$

(10)

When using non-uniform grid, however, Eq. (10) will still introduce certain numerical errors. To improve the accuracy of volume approximation, we propose a method based on the background grid. The main idea of the method is to split the associated domain of point $\boldsymbol{x}_j$ into many sub-domains based on the background grid, calculate the volume fraction of each sub-domain covered by the horizon of point $\boldsymbol{x}_i$ with Eq. (10), and summate the
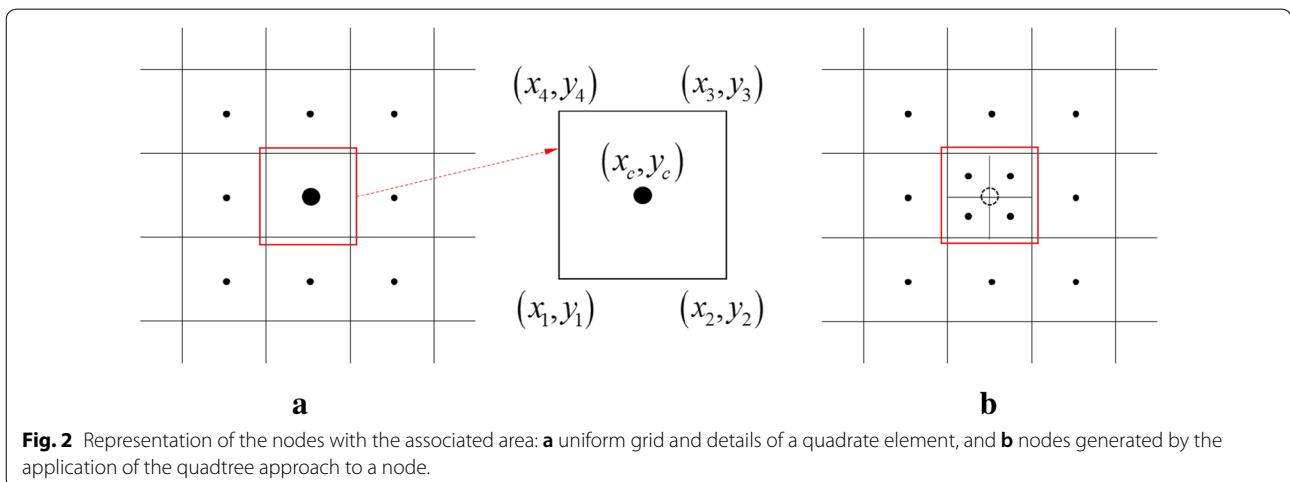

Fig. 2 Representation of the nodes with the associated area: **a** uniform grid and details of a quadrate element, and **b** nodes generated by the application of the quadtree approach to a node.

covered volumes of all sub-domains. The summation is the portion of the volume of point x_j covered by the horizon of point x_i.

Take the grid with 2 levels in Fig. 3a as an example. First, all the points at level 0 are refined to level 1 points and the inheritance relationship between old and new points are recorded. Then, the grid with all level 1 points (the blue dashed lines in Fig. 3b) is the background grid. With the background grid, calculating the volume fraction ΔV_j of point x_j covered by the horizon of point x_i is actually to calculate and summate the covered volume of all sub-domains. In the same way, the covered volume of other points could be obtained. It is a remarkable fact that the points x_j, x_k, x_m, x_n are out of the horizon of point x_i, and their distances from point x_i are more than $\delta + 0.5\Delta x$. If only Eq. (10) is utilized without the background grid, the covered volume of the four points (the black shadows in Fig. 3b) are zero, which will trigger large errors. Furthermore, the denser the background grid is, the more accurate the volume approximation is; contradictorily, the more expensive the computational cost is. Therefore, to balance the accuracy and efficiency, the background grid in level $(k+1)$ is used to calculate the volume covered by the horizon of point x_i in level k in the following simulations.

3.2.2 Solving Algorithms for Quasi-Static Problem
In its original formulation, PD has been developed to solve dynamic problems, such as dynamic crack propagation in brittle materials. In recent years, some researchers have applied PD in static problems with two methods. Kilic and Madenci (2010), Huang et al. (2015) introduced an adaptive dynamic relaxation method into

the PD equations of motion for quasi-static fracture analysis. Gerstle et al. (2007), Zaccariotto et al. (2015) converted the PD equations of motion into equilibrium equations by letting the acceleration be zero, and solved the equilibrium equations in the framework of FEM. The former method is time-consuming and the computational efficiency and accuracy is dependent on the artificial damping. In present study, truss elements are used to represent the bonds and dual-bonds, and the quasi-static simulations are carried out by solving the equilibrium equations.

In the case of quasi-static motion, the acceleration is zero. Hence, Eq. (9) is rewritten into Eq. (11) or Eq. (12) in the form of FEM.

$$\sum_{j}^{N_{H_x}} \boldsymbol{f}_{ij}(\boldsymbol{\eta}, \boldsymbol{\xi}, t)\Delta V_j + \sum_{j}^{N_{H'_x}} \left(-\boldsymbol{f}_{ji}(-\boldsymbol{\eta}, -\boldsymbol{\xi}, t)\Delta V_j \right) + \boldsymbol{b}(\boldsymbol{x}_i) = 0$$

(11)

$$[K]\{\boldsymbol{u}\} = \{\boldsymbol{F}\}$$

(12)

where $[K]$ is the global stiffness matrix, $\{\boldsymbol{u}\} = [u_1, v_1, \cdots u_i, v_i, \cdots u_n, v_n]^T$ is the vector of nodal displacements and n is the number of material points, $\{\boldsymbol{F}\} = [f_{1x}, f_{1y}, \cdots f_{ix}, f_{iy}, \cdots f_{nx}, f_{ny}]^T$ is the vector of external forces, in which $f_{ix} = b_{ix}\Delta V_i$.

$\left[\bar{k}^p\right]^e$ and $[k^p]^e$ are the element stiffness matrix of the bond $x_i x_j$ in local and global coordinates, respectively; and take the forms of

$$\left[\bar{k}^p\right]^e = \frac{c_{ij}}{||\xi_{ij}||} \begin{bmatrix} 1 & 0 & -1 & 0 \\ 0 & 0 & 0 & 0 \\ -1 & 0 & 1 & 0 \\ 0 & 0 & 0 & 0 \end{bmatrix}$$

(13)

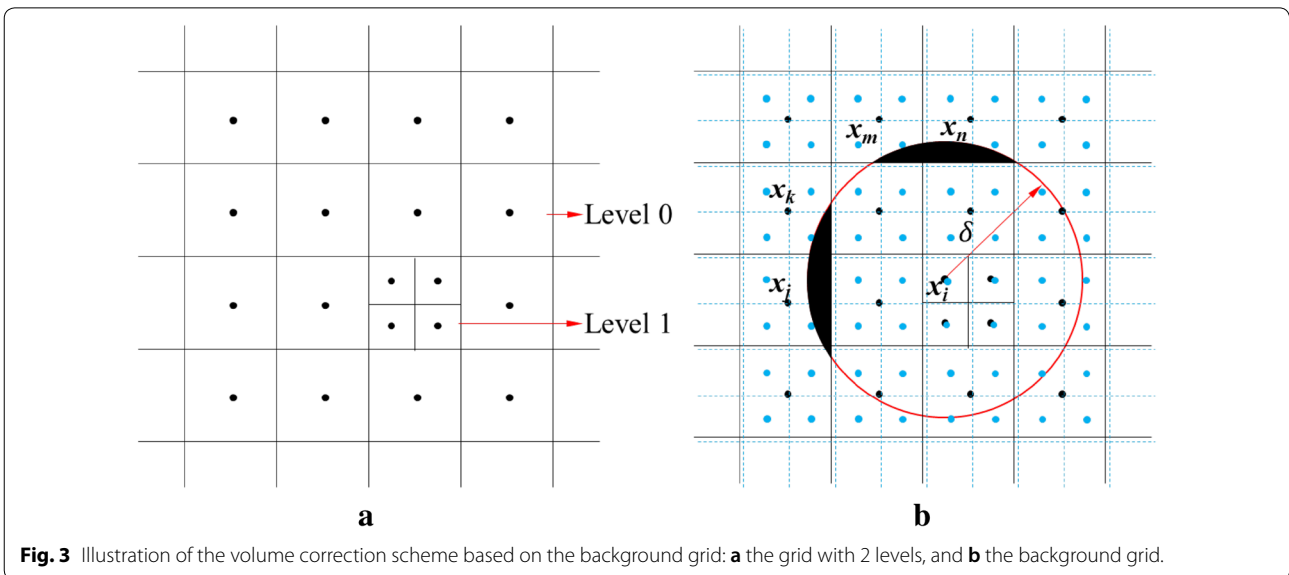**Fig. 3** Illustration of the volume correction scheme based on the background grid: **a** the grid with 2 levels, and **b** the background grid.

$$\left[k^p\right]^e = \left[T^e\right]^{\mathrm{T}}\left[\bar{k}^p\right]^e\left[T^e\right] = \frac{c_{ij}}{\|\xi_{ij}\|}\begin{bmatrix} l^2 & lm & -l^2 & -lm \\ lm & m^2 & -lm & -m^2 \\ -l^2 & -lm & l^2 & lm \\ -lm & -m^2 & lm & m^2 \end{bmatrix} = \begin{bmatrix} k_{ii}^p & k_{ij}^p \\ k_{ji}^p & k_{jj}^p \end{bmatrix} \tag{14}$$

where $[T^e]$ is the coordinate transformation matrix.

$$[T^e] = \begin{bmatrix} l & m & 0 & 0 \\ -m & l & 0 & 0 \\ 0 & 0 & l & m \\ 0 & 0 & -m & l \end{bmatrix}, \quad \begin{cases} l = (x_j - x_i)/\|\xi_{ij}\| \\ m = (y_j - y_i)/\|\xi_{ij}\| \end{cases} \tag{15}$$

The pairwise force functions of the bond x_ix_j and the dual-bond x_jx_i take the following forms

$$\begin{cases} \mathbf{f}_{ij}(\boldsymbol{\eta},\xi,t) = \quad \mu(t,\xi)[k^p]^e\{\mathbf{u}^p\}^e \\ \mathbf{f}_{ji}(-\boldsymbol{\eta},-\xi,t) = \mu(t,\xi)[k^q]^e\{\mathbf{u}^q\}^e \end{cases} \tag{16}$$

where $[k^p]^e$, $\{\mathbf{u}^p\}^e$, $[k^q]^e$ and $\{\mathbf{u}^q\}^e$ denote element stiffness matrix and the vector of element nodal displacements of the bond x_ix_j and the dual-bond x_jx_i in global coordinates, respectively.

The global stiffness matrix $[K]$ can be assembled by the superimposing method in FEM. Let row $(2i-1)$ and $(2i)$ about point x_i in $[K]$ be $[K_i]$, which can be expressed as

$$K_i = [K_{i1}, \cdots K_{ii}, \cdots K_{ij}, \cdots K_{in}] \tag{17}$$

$$K_{ii} = \sum_p^{N_{H_x}} k_{ii}^p \Delta V_i \Delta V_j + \sum_q^{N_{H_x'}} k_{ii}^q \Delta V_i \Delta V_j \tag{18a}$$

$$K_{ij} = k_{ij}^p \Delta V_i \Delta V_j + k_{ij}^q \Delta V_i \Delta V_j \tag{18b}$$

An in-house 2D peridynamic code in MATLAB is used to solve the equilibrium equations. With the micro-elastic damage model described in Eq. (5), damage is incorporated into the model. Once its critical stretch is reached, the bond fails and the global stiffness matrix is updated.

4 Simulation of the Shear Test in FRP-to-Concrete Bonded Joints

4.1 DH-PD Modeling
As a new approach in analysis of the bond behavior between FRP and concrete, the validity and accuracy of the proposed DH-PD approach need to be verified. Similar to the reliability-based analysis with a large database of joint tests in literatures (Zhang et al.

2018; Shi et al. 2015), the single shear tests reported in Yao et al. (2005) were employed to compare with the DH-PD predictions. Yao et al. (2005) reported a total of 72 tests, but 16 of them failed in other modes rather than debonding in concrete and 4 of them were designed to investigate the effect of the loading offset so they were excluded in present study. The reported specimens had two kinds of FRP (CFRP and GFRP), the FRP width ranging from 25 to 100 mm, the bond length increasing from 75 to 240 mm, concrete cylinder strength varying from 19 to 27 MPa and the height of free concrete edge changing from 5 to 120 mm. As shown in Fig. 4, a concrete prism bonded with an FRP plate was adopted in the DH-PD simulations, in which the geometry of the concrete prism was 350 mm $(L) \times 150$ mm (H), and h_c ranged from 5 to 120 mm. In the numerical model, the specimen was restrained vertically along the base and horizontally along part of the right edge. To reduce the computational cost, the three dimensional specimen was modeled as a plane stress problem and the non-uniform grid was adopted in present study. The grid spacing of concrete increases from the top to the bottom of the concrete prism, and the maximum and minimum grid spacing were 1 mm and 0.125 mm, respectively. The grid spacing of the adhesive layer and FRP plate was 0.0625 mm and 0.03125 mm, respectively. The material properties for specimens were given in Table 1.

In order to correctly model real materials, some material properties have to be mathematically transformed to equivalent parameters used in DH-PD. The micro-modulus of bonds in FRP, the adhesive layer and concrete could be obtained from Eq. (3). The critical stretch of each phase is equal to the corresponding ultimate tensile strain. It is worth noting that the material model of DH-PD bonds in all three phases is assumed to be linearly elastic brittle. Once the critical stretch is exceeded, the bond is broken and removed from the analysis.

4.2 Comparison of DH-PD Predictions with Test Results
In present study, the shear test was modeled as a plane stress problem, while the actual behavior is three-dimensional. Therefore, the width ratio factor β_w proposed by Chen and Teng (2001) was adopted to correct the discrepancy. The predicted load, displacement, stress and
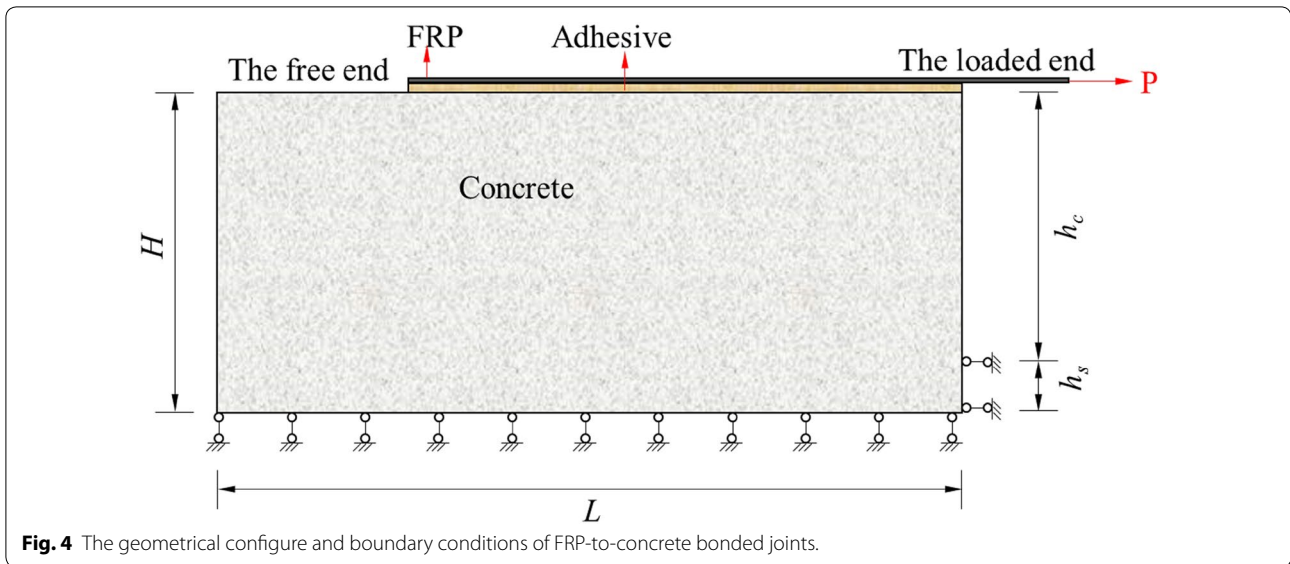
Fig. 4 The geometrical configure and boundary conditions of FRP-to-concrete bonded joints.

Table 1 Material properties of each phase in FRP-to-concrete bonded joints (Yao et al. 2005; Bai 2013).

Material	Thickness (mm)	Tensile strength (MPa)	Elastic modulus (GPa)	Ultimate tensile strain (%)
CFRP	0.165	4114	256	1.61
GFRP	1.27	351	22.5	1.56
Adhesive	1	60	2	3
Concrete	150	1.01–1.89	23.9–34.3	0.00423–0.00551

strain in the FRP plate were all adjusted with the width ratio factor β_w. The width ratio factor took the form of

$$\beta_w = \sqrt{\frac{2 - b_f/b_c}{1 + b_f/b_c}} \tag{19}$$

where b_f and b_c are the widths of the FRP plate and the concrete prism, respectively.

Figure 5 shows the comparison of DH-PD predictions with test results. It can be clearly seen that the DH-PD predicted results are overall in very close agreement with the 52 test data. The typical specimen (specimen II-5) is chosen from the aforementioned database for further comparison between the DH-PD prediction, test data, FEM results and the analytical solution.

Damage contour of debonding failure for specimen II-5 is shown in Fig. 6, in which only the part of concrete near the adhesive-to-concrete interface is exhibited for easier observation. It can be observed that debonding failure occurs in concrete at a small distance (1–4 mm) beneath
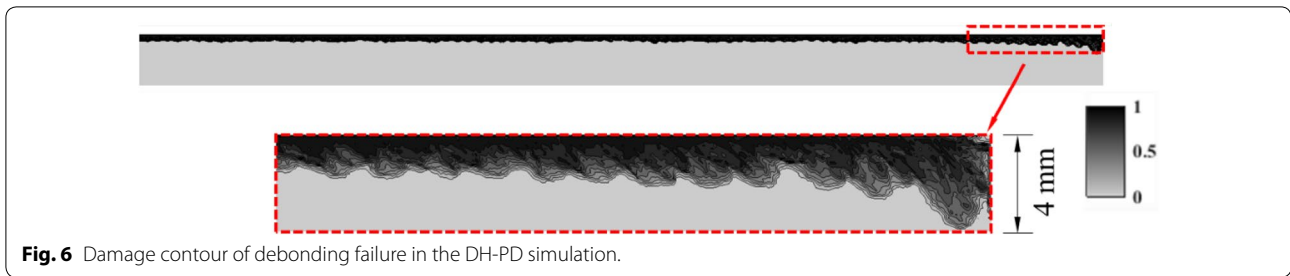

Fig. 5 Comparison of the DH-PD predictions with test results.

Fig. 6 Damage contour of debonding failure in the DH-PD simulation.

the adhesive-to-concrete interface. Additionally, the distribution of damage is not uniform along the bond interface and the cracks are at about 45° to the horizontal. These phenomena are consistent with the experimental observations (Yao et al. 2005; Ali-Ahmad et al. 2006; Carrara et al. 2011; Benzarti et al. 2011; Wu and Jiang 2013) and the FEM results (Lu et al. 2005a, 2006; Pham and Al-Mahaidi 2007; Tao and Chen 2015; Xu et al. 2015).

A comparison of the load–displacement curves for specimen II-5 between the experiment, the FEM simulation, the analytical solution and present simulation is shown in Fig. 7. It is clear that the numerically predicted response agrees well with the experimental and FEM results. Point A and B marked on the curves represent the softening initiation and the debonding initiation, respectively. Initially, the load increases linearly with the displacement until Point A is reached. Subsequently, the concrete under the adhesive-to-concrete interface near

the loaded end exhibits damage and the softening phase initializes. When Point B is reached, the FRP starts to debond from concrete and thereafter the debonding propagates rapidly towards the free end of the FRP. It is worth noting that, similar to the trend of the experimental and FEM results, the load increases slowly after the debonding initiation, which is probably caused by the friction in the debonded zone and the stochastic nature of the cracking process.

Figure 8 shows the normal stress distributions of FRP plate in the experiment, the FEM simulation, the analytical study, and present DH-PD simulation at Point A, B and C marked in Fig. 7. There is a very close agreement between the four curves at Point A. At Point B and C, the DH-PD predictions are consistent with the FEM and analytical curves and in agreement with the experimental results in terms of the overall trend, despite the large fluctuations in the experimental results. Fig 9 shows the
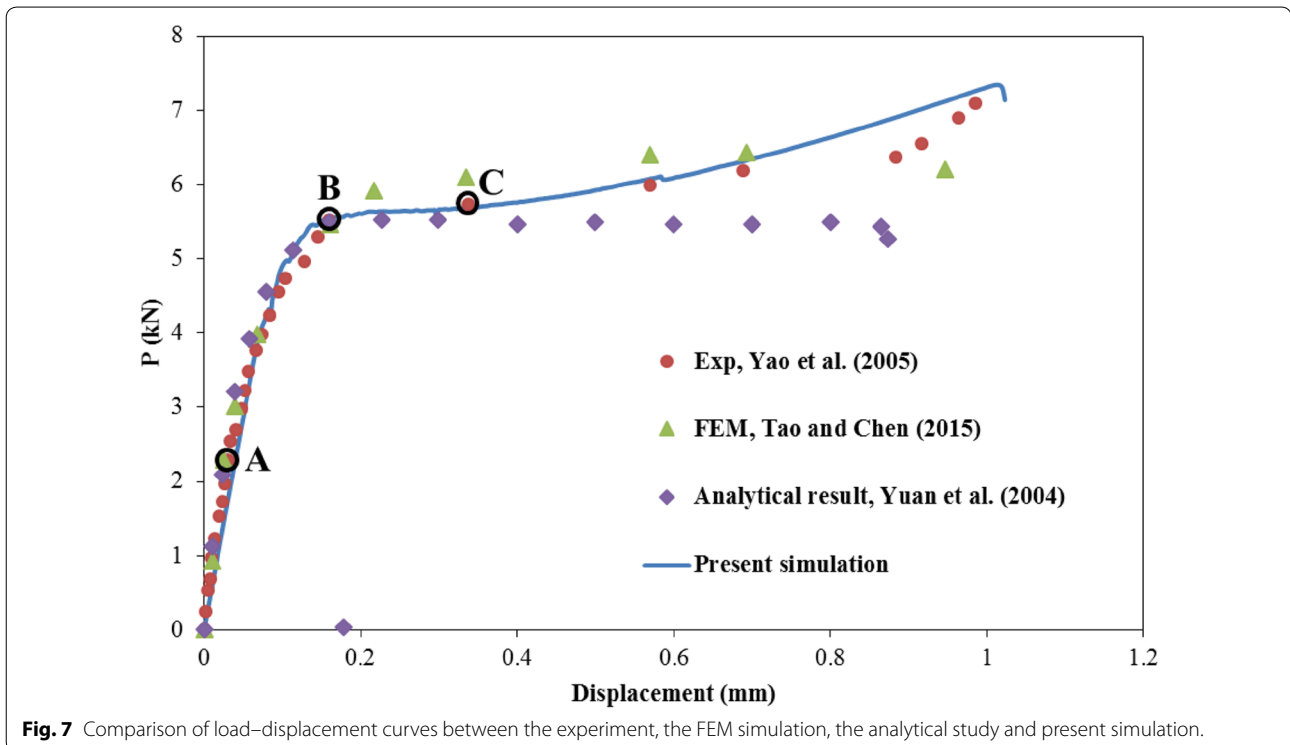

Fig. 7 Comparison of load–displacement curves between the experiment, the FEM simulation, the analytical study and present simulation.
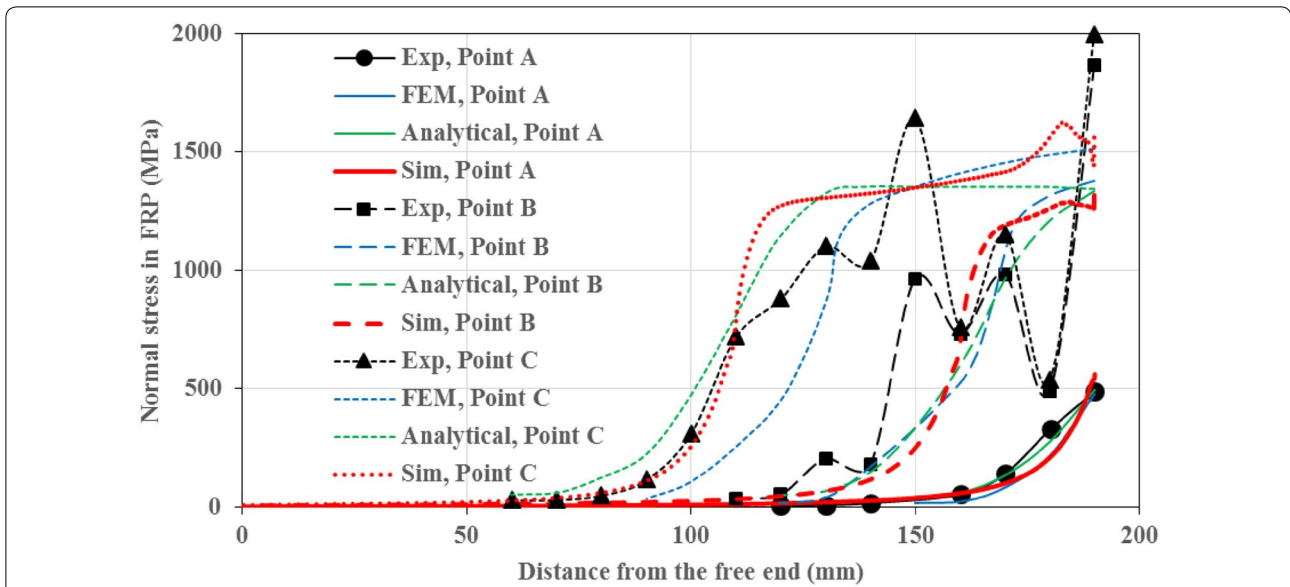
Fig. 8 Normal stress distributions in FRP plate of the experiment in Yao et al. (2005), the FEM simulation in Tao and Chen (2015), the analytical solution in Yuan et al. (2004) and present simulation.
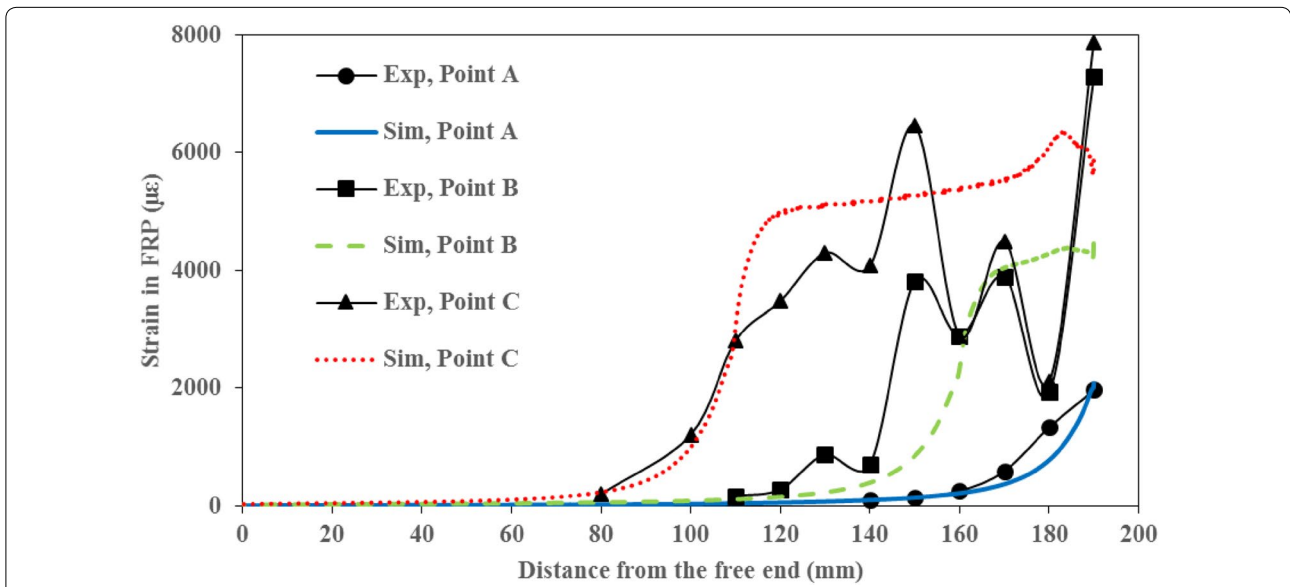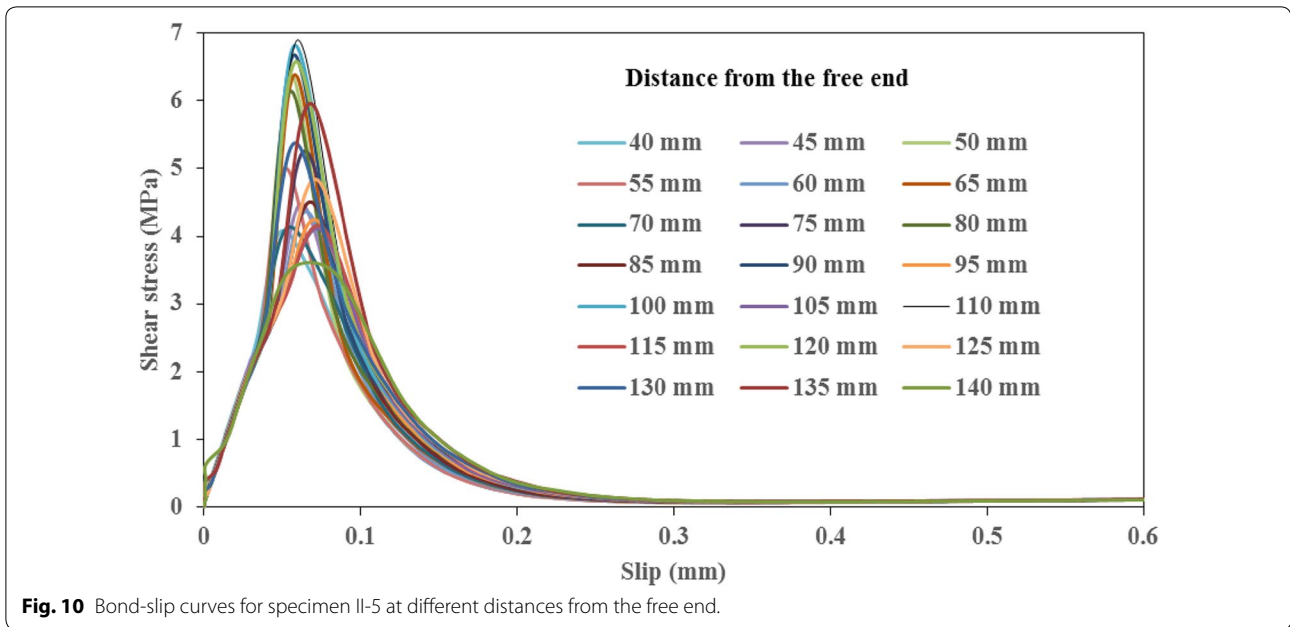

Fig. 9 Comparison of normal strain distributions in FRP plate between present simulation and the experiment in Yao et al. (2005).

comparison of the normal strain distributions in FRP plate between the experiment and present simulation. Similar to the normal stress, the DH-PD predictions are in agreement with the experimental results in overall trend and the test strain fluctuates as a result of probable measurement errors and plate bending due to the thinness of the plate and the roughness along the crack.

Bond-slip curves for specimen II-5 at different distances from the free end are shown in Fig. 10, in which the interfacial slip of a particular point is defined as the relative displacement between the FRP plate and concrete at that point, and the shear stress at the corresponding location of the interface is calculated from the normal stress in the FRP plate using the following relationship (Wu and Jiang 2013; Dai et al. 2005; Lu et al. 2005a; Nakaba et al. 2001)
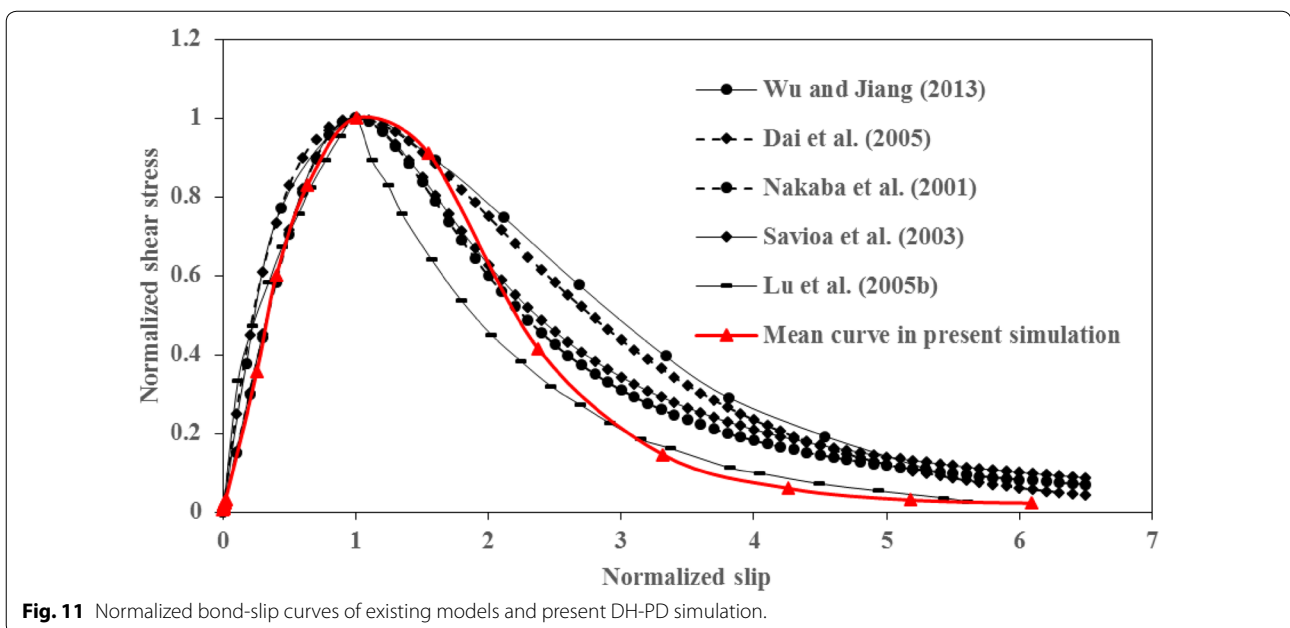
$$\tau(x) = t_f \frac{\sigma_f(x + \mathrm{d}x/2) - \sigma_f(x - \mathrm{d}x/2)}{\mathrm{d}x} \tag{20}$$

Fig. 10 Bond-slip curves for specimen II-5 at different distances from the free end.

where σ_f and t_f are the normal stress and the thickness of the FRP plate, respectively; x is the distance from the free end; dx is the incremental distance used for calculation of the shear stress.

It can be seen from Fig. 10 that the trends of bond slip curves at different distances from the free end are consistent, while the numerical difference of the maximum shear stresses is large. The non-uniform bond-slip relationship is in accordance with the test findings (Dai et al. 2005; Chajes et al. 1996; Yun et al. 2008), the

FEM result (Lin and Wu 2016) and the analytical study (Zhou et al. 2010). The non-uniformity is related to the variation of the depth of failure plane. When the failure depth increases, the maximum shear stress increases (Lin and Wu 2016). To further verify the accuracy of the bond-slip relationship, the mean curve of all curves in Fig. 9 is calculated and compared with existing bond-slip models. It can be observed from Fig. 11 that the mean curve predicted by DH-PD simulation matches well with existing bond-slip models(Wu and Jiang 2013;

Fig. 11 Normalized bond-slip curves of existing models and present DH-PD simulation.

Dai et al. 2005; Nakaba et al. 2001; Savoia et al. 2003; Lu et al. 2005b).

5 Discussion

As mentioned above, the main failure mode of FRP-to-concrete bonded joints in the shear tests is concrete failure. Therefore, the mechanical performances of concrete play a dominant role in the bond behavior. Additionally, the bond behavior can be also affected by the geometric and material properties of FRP and the adhesive. In this section, the effects of concrete strength, the thickness of the FRP plate and the adhesive layer on the bond behavior were studied with the proposed DH-PD model.

5.1 Effect of Concrete Strength

In order to investigate the effect of concrete strength on the bond behavior, four groups of DH-PD models for specimen II-5 with concrete strengths ranging from C20 to C50 were adopted. From C20 to C50, the tensile strength is 1.1 MPa, 1.43 MPa, 1.71 MPa, 1.89 MPa, and the elastic modulus is 25.5 GPa, 30 GPa, 32.5 GPa, 34.5 GPa, respectively.

Figure 12 illustrates the load–displacement curves with different concrete strengths. It is evident that the ultimate load and the debonding ductility increase with the increasing concrete strength. It has been generally accepted that the debonding failure occurs in concrete and thus the bond behavior is usually controlled by the behavior of concrete. Higher concrete strength contributes to stronger resistance to debonding, and
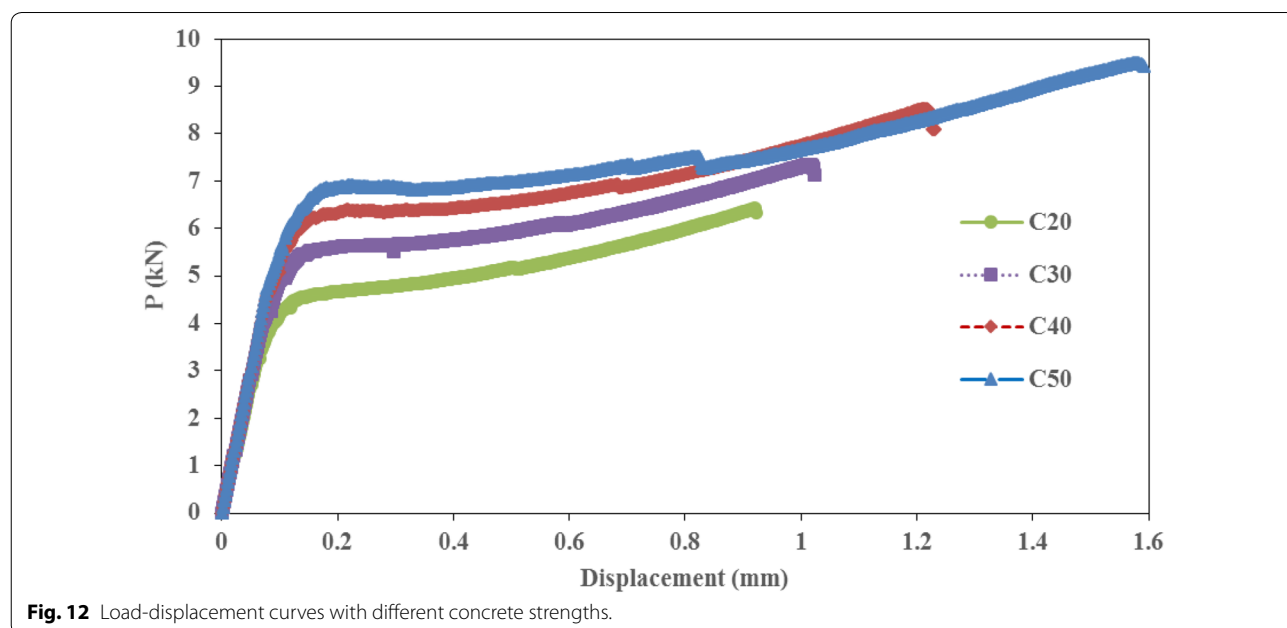
consequently the ultimate load and the debonding ductility are higher. Furthermore, the maximum shear stress at a particular point of the interface denotes the bond strength at that point. The average maximum shear stress of all material points in the interface versus concrete strength is shown in Fig. 13. It can be observed that the average maximum shear stress almost increases linearly with concrete strength, which demonstrates that the bond strength increases with the increasing concrete strength.
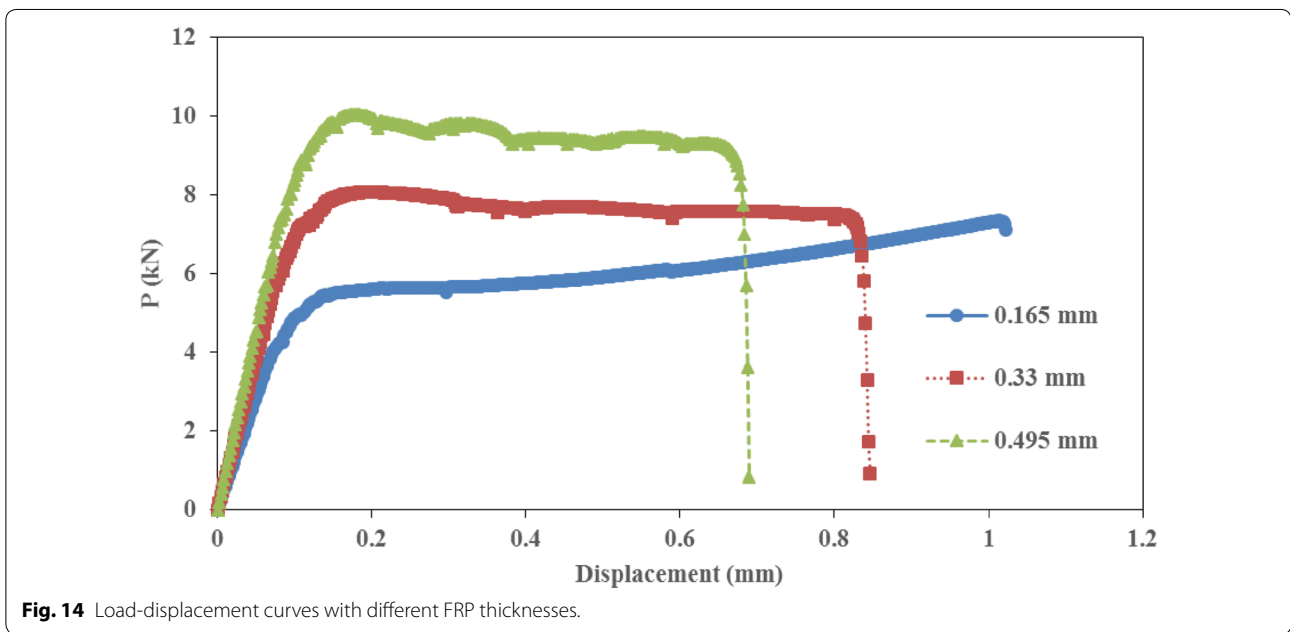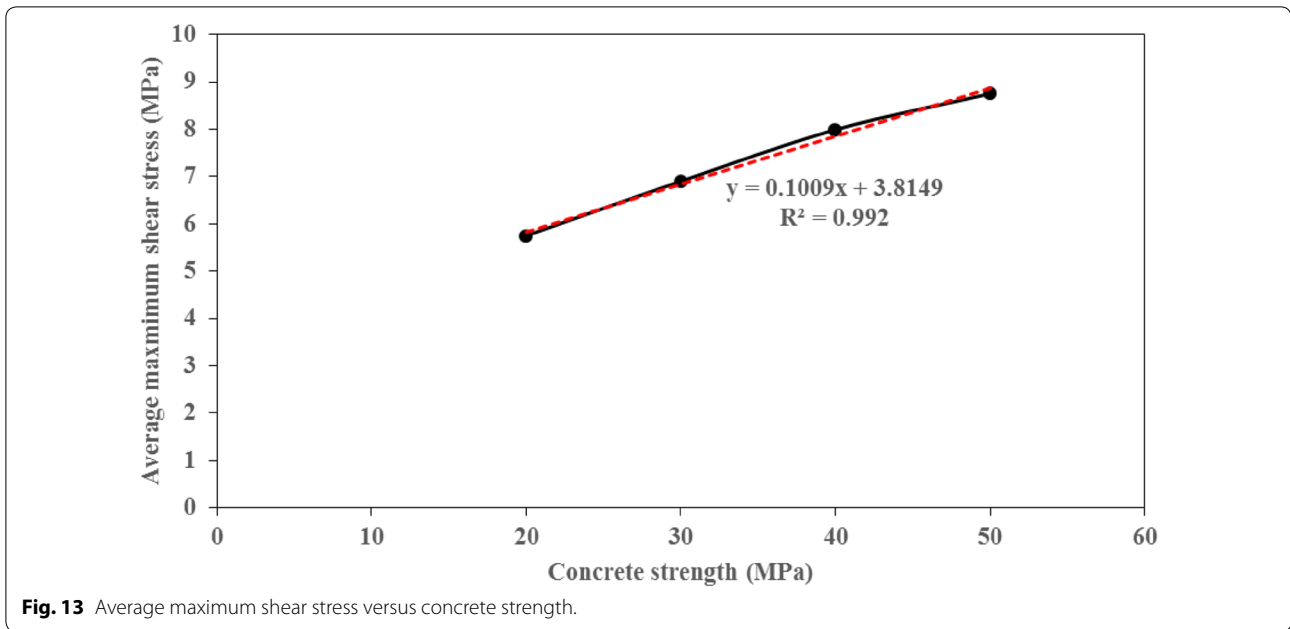
5.2 Effect of the Thickness of FRP Plate and Adhesive Layer

To study the effect of the FRP thickness on the bond behavior, three groups of DH-PD models with different FRP thicknesses (0.165 mm, 0.33 mm and 0.495 mm) were adopted.

Figure 14 shows the load–displacement curves with different FRP thicknesses. It can be clearly seen that the ultimate load increases with the increasing FRP thickness, while the debonding ductility significantly decreases. These phenomena match well with the test results (Zhang and Smith 2013) and the numerical simulations (Sun et al. 2017a, b), which further demonstrates the accuracy and efficiency of the proposed DH-PD model. Additionally, the decrease of the debonding ductility indicates that the efficiency of the FRP plate is reduced when a thicker FRP plate is used.

Figure 15 illustrates the predicted load–displacement curves with different adhesive thickness, in which

Fig. 12 Load-displacement curves with different concrete strengths.

Fig. 13 Average maximum shear stress versus concrete strength.

Fig. 14 Load-displacement curves with different FRP thicknesses.
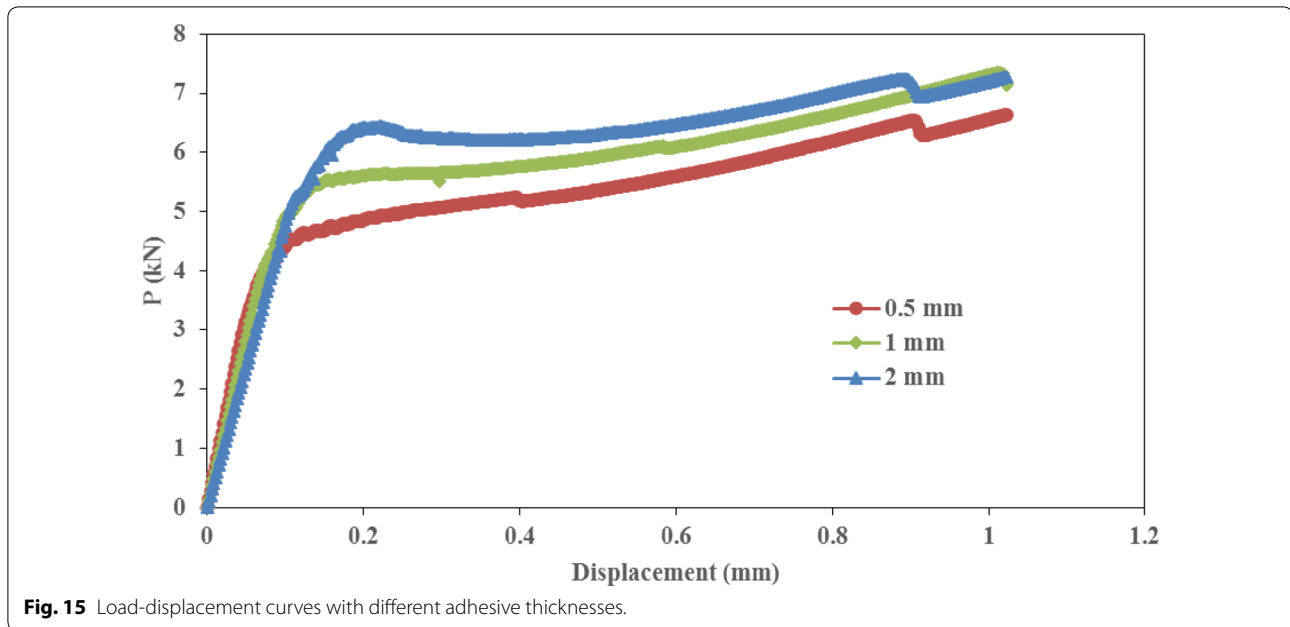
the adhesive thicknesses are 0.5 mm, 1 mm and 2 mm, respectively. As shown in Fig. 15, the ultimate load slightly increase with the adhesive thickness. In addition, the average maximum shear stresses for the three adhesive thicknesses have small difference and are 6.82 MPa, 6.9 MPa and 6.96 MPa, respectively; that is, the adhesive thickness has no significant effect on the bond strength. Therefore, the effect of the adhesive layer can be regarded as mainly playing a role in transferring surely shear stresses from concrete to the FRP plate.

6 Conclusions

A DH-PD model implemented in the framework of FEM with multi-scale discretization and a volume correction scheme have been developed for the simulation of debonding process in FRP-to-concrete bonded joints in this paper. A benchmark numerical example was implemented to validate the proposed model in the analysis of the debonding process. The predicted results including concrete failure pattern, load-slip curve, FRP stress distribution, FRP strain distribution were consistent with

Fig. 15 Load-displacement curves with different adhesive thicknesses.

the experimental findings, the FEM simulations and the analytical solutions. Furthermore, the effects of concrete strength, the FRP thickness and the adhesive thickness on the bond behavior were investigated. The main conclusions could be drawn as follows.

1. The DH-PD model of FRP-to-concrete bonded joints combines the efficiency of FEM with the generality of DH-PD, and thus can effectively simulate the debonding process. The model lays a certain foundation for further research of the bond behavior.
2. The non-uniform discretization generated from the quadtree approach can significantly reduce the computational cost. The volume correction scheme based on the background grid can enhance the accuracy when the non-uniform grid is used. Moreover, the utilization of the background grid need to balance the accuracy and efficiency.
3. The concrete failure pattern and the local bond strength along the interface is non-uniform. The non-uniformity is consistent with the experimental observations, which probably caused by the friction in the debonded zone and the stochastic nature of the cracking process.
4. The bond strength and the debonding ductility are distinctly affected by concrete strength and the FRP thickness, while the adhesive thickness has no significant effect on the bond behavior. The bond strength and the debonding ductility increase with the increasing concrete strength. For a thicker FRP plate,

the bond strength will increase and the debonding ductility will decrease.

Publisher's Note
Springer Nature remains neutral with regard to jurisdictional claims in published maps and institutional affiliations.

References

Ali-Ahmad, M., Subramaniam, K., & Ghosn, M. (2006). Experimental investigation and fracture analysis of debonding between concrete and FRP sheets. *Journal of Engineering Mechanics, 132*(9), 914–923.

Bai, J. P. (2013). *Advanced fibre-reinforced polymer (FRP) composites for structural applications.* Cambridge: Woodhead.

Benzarti, K., Freddi, F., & Frémond, M. (2011). A damage model to predict the durability of bonded assemblies. Part I: Debonding behavior of FRP strengthened concrete structures. *Construction and Building Materials, 25*(2), 547–555.

Bobaru, F., & Duangpanya, M. (2012). A peridynamic formulation for transient heat conduction in bodies with evolving discontinuities. *Journal of Computational Physics, 231*(7), 2764–2785.

Bobaru, F., & Ha, Y. D. (2011). Adaptive refinement and multiscale modeling in 2D peridynamics. *Journal for Multiscale Computational Engineering, 9*(6), 635–659.

Bobaru, F., Yang, M. J., Alves, L. F., Silling, S. A., Askari, E., & Xu, J. F. (2009). Convergence, adaptive refinement, and scaling in 1D peridynamics. *International Journal for Numerical Methods in Engineering, 77*(6), 852–877.

Carrara, P., Ferretti, D., Freddi, F., & Rosati, G. (2011). Shear tests of carbon fiber plates bonded to concrete with control of snap-back. *Engineering Fracture Mechanics, 78*(15), 2663–2678.

Chajes, M. J., Finch, W. W., & Thomson, T. A. (1996). Bond and force transfer of composite-material plates bonded to concrete. *ACI Structure Journal, 93*(2), 209–217.

Chen, G. M., Teng, J. G., & Chen, J. F. (2011). Finite-element modeling of intermediate crack debonding in FRP-plated RC beams. *Journal of Composites for Construction, 15*(3), 339–353.

Chen, J. F., & Teng, J. G. (2001). Anchorage strength models for FRP and steel plates bonded to concrete. *Journal of Structural Engineering, 127*(7), 784–791.

Chen, J. F., Yang, Z. J., & Holt, G. D. (2001). FRP or steel plate-to-concrete bonded joints: Effect of test methods on experimental bond strength. *Steel and Composite Structures, 1*(2), 231–244.

Dai, J. G., Ueda, T., & Sato, Y. (2005). Development of the nonlinear bond stress-slip model of fiber reinforced plastics sheet–concrete interfaces with a simple method. *Journal of Composites for Construction, 9*(1), 52–62.

Diab, H., & Wu, Z. S. (2007). Nonlinear constitutive model for time–dependent behavior of FRP-concrete interface. *Composites Science and Technology, 67*(11–12), 2323–2333.

Dipasquale, D., Zaccariotto, M., & Galvanetto, U. (2014). Crack propagation with adaptive grid refinement in 2D peridynamics. *International Journal of Fracture, 190*(1–2), 1–22.

Gerstle, W., Sau, N., & Silling, S. A. (2007). Peridynamic modeling of concrete structures. *Nuclear Engineering and Design, 237*(12–13), 1250–1258.

Ha, Y. D., & Bobaru, F. (2011). Characteristics of dynamic brittle fracture captured with peridynamics. *Engineering Fracture Mechanics, 78*(6), 1156–1168.

Hu, W., Ha, Y. D., & Bobaru, F. (2012). Peridynamic model for dynamic fracture in unidirectional fiber-reinforced composites. *Computer Methods in Applied Mechanics and Engineering, 217–220,* 247–261.

Huang, D., Lu, G. D., Wang, C. W., & Qiao, P. Z. (2015). An extended peridynamic approach for deformation and fracture analysis. *Engineering Fracture Mechanics, 141,* 196–211.

Jabakhanji, R., & Mohtar, R. H. (2015). A peridynamic model of flow in porous media. *Advances in Water Resources, 78,* 22–35.

Kabir, M. I., Samali, B., & Shrestha, R. (2017). Pull-out strengths of GFRP-concrete bond exposed to applied environmental conditions. *International Journal of Concrete Structures and Materials, 11*(1), 69–84.

Kilic, B., & Madenci, E. (2010). An adaptive dynamic relaxation method for quasi-static simulations using the peridynamic theory. *Theoretical and Applied Fracture Mechanics, 53*(3), 194–204.

Li, W. J., & Guo, L. (2018). Meso-fracture simulation of cracking process in concrete incorporating three-phase characteristics by peridynamic method. *Construction and Building Materials, 161,* 665–675.

Lin, J. P., & Wu, Y. F. (2016). Numerical analysis of interfacial bond behavior of externally bonded FRP-to-concrete bonded joints. *Journal of Composites for Construction, 20*(5), 04016028.

Liu, K., & Wu, Y. F. (2012). Analytical identification of bond-slip relationship of EB-FRP joints. *Composites Part B Engineering, 43*(4), 1955–1963.

Lu, X. Z., Jiang, J. J., Teng, J. G., & Ye, L. P. (2006). Finite element simulation of debonding in FRP-to-concrete bonded joints. *Construction and Building Materials, 20*(6), 412–424.

Lu, X. Z., Ye, L. P., Teng, J. G., & Jiang, J. J. (2005a). Meso-scale finite element model for FRP sheets/plates bonded to concrete. *Engineering Structures, 27*(4), 564–575.

Lu, X. Z., Ye, L. P., Teng, J. G., & Jiang, J. J. (2005b). Bond-slip models for FRP sheets/plates bonded to concrete. *Engineering Structures, 27*(6), 920–937.

Macek, R. W., & Silling, S. A. (2007). Peridynamics via finite element analysis. *Finite Elements in Analysis and Design, 43*(15), 1169–1178.

Moein, R. S., & Tasnimi, A. A. (2016). An analytical model for FRP debonding in strengthened RC beams under monotonic and cyclic loads. *International Journal of Concrete Structures and Materials, 10*(4), 499–511.

Nakaba, K., Kanakubo, T., Furuta, T., & Yoshizawa, H. (2001). Bond behavior between fiber-reinforced polymer laminates and concrete. *ACI Structural Journal, 98*(3), 359–367.

Pan, J. L., & Wu, Y. F. (2014). Analytical modeling of bond behavior between FRP plate and concrete. *Composites Part B Engineering, 61*(5), 17–25.

Pham, H. B., & Al-Mahaidi, R. (2007). Modelling of CFRP-concrete shear-lap tests. *Construction and Building Materials, 21*(4), 727–735.

Rabczuk, T., & Ren, H. L. (2017). A peridynamics formulation for quasi-static fracture and contact in rock. *Engineering Geology, 225,* 42–48.

Ren, H. L., Zhuang, X. Y., Cai, Y. C., & Rabczuk, T. (2016). Dual-horizon peridynamics. *International Journal for Numerical Methods in Engineering, 108*(12), 1451–1476.

Ronagh, H. R., & Baji, H. (2014). On the FE modeling of FRP-retrofitted beam-column subassemblies. *International Journal of Concrete Structures and Materials, 8*(2), 141–155.

Savoia, M., Ferracuti, B., & Mazzotti, C. (2003). Non-linear bond-slip law for FRP-concrete interface. *In Fibre-Reinforced Polymer Reinforcement for Concrete Structures,* World Scientific Publications, Singapore.

Shi, J. W., Wu, Z. S., Wang, X., & Noori, M. (2015). Reliability analysis of intermediate crack-induced debonding failure in FRP-strengthened concrete members. *Structure and Infrastructure Engineering, 11*(12), 1651–1671.

Silling, S. A. (2000). Reformulation of elasticity theory for discontinuities and long-range forces. *Journal of the Mechanics and Physics of Solids, 48*(1), 175–209.

Silling, S. A., & Askari, E. (2005). A meshfree method based on the peridynamic model of solid mechanics. *Computers & Structures, 83*(17–18), 1526–1535.

Silling, S. A., Epton, M., Weckner, O., Xu, J., & Askari, E. (2007). Peridynamic states and constitutive modeling. *Journal of Elasticity, 88*(2), 151–184.

Sun, W., Peng, X., Liu, H. F., & Qi, H. P. (2017a). Numerical studies on the entire debonding propagation process of FRP strips externally bonded to the concrete substrate. *Construction and Building Materials, 149,* 218–235.

Sun, W., Peng, X., & Yu, Y. (2017b). Development of a simplified bond model used for simulating FRP strips bonded to concrete. *Composite Structures, 171,* 462–472.

Täljsten, B. (1996). Strengthening of concrete prisms using the plate-bonding technique. *International Journal of Fracture, 82*(3), 253–266.

Tao, Y., & Chen, J. F. (2015). Concrete damage plasticity model for modeling FRP-to-concrete bond behavior. *Journal of Composites for Construction, 19*(1), 04014026.

Wu, Y. F., & Jiang, C. (2013). Quantification of bond-slip relationship for externally bonded FRP-to-concrete bonded joints. *Journal of Composites for Construction, 17*(5), 673–686.

Xu, T., He, Z. J., Tang, C. A., Zhu, W. C., & Ranjith, P. G. (2015). Finite element analysis of width effect in interface debonding of FRP plate bonded to concrete. *Finite Elements in Analysis and Design, 93,* 30–41.

Yao, J., Teng, J. G., & Chen, J. F. (2005). Experimental study on FRP-to-concrete bonded joints. *Composites Part B Engineering, 36*(2), 99–113.

Yuan, H., Teng, J. G., Seracino, R., Wu, Z. S., & Yao, J. (2004). Full-range behavior of FRP-to-concrete bonded joints. *Engineering Structures, 26*(5), 553–565.

Yun, Y. C., Wu, Y. F., & Tang, W. C. (2008). Performance of FRP bonding systems under fatigue loading. *Engineering Structures, 30*(11), 3129–3140.

Zaccariotto, M., Luongo, F., Sarego, G., & Galvanetto, U. (2015). Examples of applications of the peridyanmic theory to the solution of static equilibrium problems. *The Aeronautical Journal, 119*(1216), 677–700.

Zhang, D. M., Gu, X. L., Yu, Q. Q., Huang, H. W., Wan, B. L., & Jiang, C. (2018). Fully probabilistic analysis of FRP-to-concrete bonded joints considering model uncertainty. *Composite Structures, 185,* 786–806.

Zhang, H. W., & Smith, S. T. (2013). Fiber-reinforced polymer (FRP)-to-concrete joints anchored with FRP anchors: test and experimental trends. *Canadian Journal of Civil Engineering, 40*(11), 1103–1116.

Zhou, Y. W., Wu, Y. F., & Yun, Y. C. (2010). Analytical modeling of the bond–slip relationship at FRP-concrete interfaces for adhesively-bonded joints. *Composites Part B Engineering, 41*(6), 423–433.